

Supporting Information for

Four-Step Thermosensitive Dielectric Response Arising from Motionable Low-Symmetry Ammonium Confined in Deformable Supramolecular Cages

Zhi-Hui Jia,^a Jing-Yan Liu,^b De-Xuan Liu,^c Shi-Yong Zhang,^b Zi-Yi Du,^{*a} Chun-Ting He,^{*a} Wei-Xiong Zhang,^{*c} and Xiao-Ming Chen^c

^a*College of Chemistry and Chemical Engineering, MOE Key Laboratory of Functional Small Organic Molecule, Jiangxi Normal University, Nanchang 330022, China.*

^b*College of Chemistry and Chemical Engineering, Gannan Normal University, Ganzhou 341000, China.*

^c*School of Chemistry, MOE Key Laboratory of Bioinorganic and Synthetic Chemistry, Sun Yat-Sen University, Guangzhou 510275, China.*

**Correspondence to: Zi-Yi Du, E-mail: ziyidu@gmail.com. Chun-Ting He, E-mail: hct@jxnu.edu.cn.*

Wei-Xiong Zhang, E-mail: zhanqwx6@mail.sysu.edu.cn.

Index

Table S1 Summary of crystal data and structural refinement for **1** at the three phases

Table S2 Selected bond lengths (Å) for **1** at the three phases

Table S3 The S...S contacts (Å) in **1** at the three phases

Table S4 The fitting parameters of the doubly superimposed Havriliak–Negami equation for **1** at specific temperatures

Chart S1 Evolution of the supramolecular cage types with variable free volumes in the four phases of **1**

Fig. S1 Room-temperature powder XRD patterns of **1**

Fig. S2 Final Rietveld refinement result for **1λ** phase at 393 K

Fig. S3 Thermogravimetric curve of **1**

Fig. S4 In situ above-room-temperature DSC measurement for **1** recorded on variable heating/cooling rates of 1, 3, 5 and 10 K/min, respectively.

Fig. S5 ORTEP representations of the selected unit of **1** at 120 K (a), 180 K (b), and 296 K (c), respectively. For comparison, the overlay map of the $[\text{Ni}(\text{NCS})_6]^{4-}$ anions in three phases is shown in (d)

Fig. S6 View of the overall stacking of **1λ** phase

Fig. S7 Comparison of the room-temperature supramolecular $\{[\text{Ni}(\text{NCS})_6]^{4-}\}_\infty$ layers in $(\text{Me}_3\text{NH})_4[\text{Ni}(\text{NCS})_6]$ (a) and **1γ** (b). From **γ** to **λ** phase, the $\{[\text{Ni}(\text{NCS})_6]^{4-}\}_\infty$ layer is broken and the $[\text{Ni}(\text{NCS})_6]^{4-}$ anions turn disordered dynamically. The significantly changed geometric arrangement of the $[\text{Ni}(\text{NCS})_6]^{4-}$ anions is shown in (c)

Fig. S8 Views of the overall stacking of **1γ** (a), **1β** (b) and **1α** phases (c), respectively

Fig. S9 Views of the stacking of the supramolecular layers of $[\text{Ni}(\text{NCS})_6]^{4-}$ anions in **1β** phase down the a-axis. The N5-, N6- and N7-containing Me_2EtNH^+ ions reside in the supramolecular cages **C**, **D** and **E**, respectively

Fig. S10 Views of the stacking of the supramolecular layers of $[\text{Ni}(\text{NCS})_6]^{4-}$ anions in **1α** phase down the a-axis. The N7-, N8-, N9- and N10-containing Me_2EtNH^+ ions reside in the supramolecular cages **F**, **G**, **H** and **I**, respectively

Fig. S11 Local snapshots of NVT dynamic simulations at 120 K for N7-containing Me_2EtNH^+ ion in **1α** phase over the simulation time (a-g), and the overlapping maps of these snapshots (h)

Fig. S12 Local snapshots of NVT dynamic simulations at 120 K for N8-containing Me_2EtNH^+ ion in **1α** phase over the simulation time (a-g), and the overlapping maps of these snapshots (h)

Fig. S13 Local snapshots of NVT dynamic simulation at 120 K for N9-containing Me_2EtNH^+ ion in **1α** phase over the simulation time (a-g), and the overlapping maps of these snapshots (h)

Fig. S14 Local snapshots of NVT dynamic simulation at 120 K for N10-containing Me_2EtNH^+ ion in **1α** phase over the simulation time (a-g), and the overlapping maps of these snapshots (h)

Fig. S15 Local snapshots of NVT dynamic simulation at 180 K for N5-containing Me_2EtNH^+ ion in 1β phase over the simulation time (a-g), and the overlapping maps of these snapshots (h)

Fig. S16 Local snapshots of NVT dynamic simulation at 180 K for N6-containing Me_2EtNH^+ ion in 1β phase over the simulation time (a-g), and the overlapping maps of these snapshots (h)

Fig. S17 Local snapshots of NVT dynamic simulation at 180 K for N7-containing Me_2EtNH^+ ion in 1β phase over the simulation time (a-g), and the overlapping maps of these snapshots (h)

Fig. S18 Local snapshots of NVT dynamic simulation at 300 K for N3-containing Me_2EtNH^+ ion in 1γ phase over the simulation time (a-g), and the overlapping maps of these snapshots (h)

Fig. S19 Local snapshots of NVT dynamic simulation at 300 K for N4-containing Me_2EtNH^+ ion in 1γ phase over the simulation time (a-g), and the overlapping maps of these snapshots (h)

Fig. S20 Overlapping maps of the snapshots for one $[\text{Ni}(\text{NCS})_6]^{4-}$ anion (a) and two N3-containing Me_2EtNH^+ ions (b, c), respectively, by first-principles NVT dynamic simulation of 1λ phase at simulation temperature of 573 K, showing orientation changes and short-range displacements over the simulation time of 0, 2, 4, 6, 8, and 10 ps

Fig. S21 The variable-temperature Cole–Cole plots as a series of arcs shown the relationship between ϵ' and ϵ'' . Based on the obtained fitting parameters, the fitted Cole–Cole diagrams of two separated relaxation processes 1 and 2 are illustrated in the inset map

Fig. S22 Variable-temperature impedance spectra for the polycrystalline pellet of **1**

Fig. S23 Variable-temperature infrared spectra of **1**

Table S1 Summary of crystal data and structural refinement for **1** at three phases

Temperature (K)	120(2)	180(2)	296(2)
Empirical formula	C ₂₂ H ₄₈ N ₁₀ S ₆ Ni ₁		
Formula weight	703.77		
Phase	α	β	γ
Space group ^[a]	<i>P2₁/n</i>	<i>Pbnm</i>	<i>Acam</i>
<i>a</i> (Å)	12.783(3)	12.8756(3)	12.9430(7)
<i>b</i> (Å)	14.478(3)	14.5845(3)	15.0014(8)
<i>c</i> (Å)	19.285(4)	19.1455(4)	19.3631(11)
θ/deg	90.207(6)	90	90
<i>V</i> /Å ³	3569.0(14)	3595.22(13)	3759.6(4)
<i>Z</i>	4	4	4
<i>D_{calcd}</i> /g cm ⁻³	1.310	1.300	1.243
μ/mm ⁻¹	0.924	0.917	0.877
GOF on F ²	1.069	1.044	1.050
<i>R</i> ₁ , <i>wR</i> ₂ [<i>I</i> > 2σ(<i>I</i>)] ^[b]	0.0508, 0.1026	0.0484, 0.1280	0.0569, 0.1624
<i>R</i> ₁ , <i>wR</i> ₂ (all data)	0.0699, 0.1150	0.0540, 0.1309	0.0816, 0.1836

^[a]To straightly compare the corresponding cell parameters, non-standard space groups for them were adopted here.

$$^{[b]}R_1 = \sum ||F_o| - |F_c|| / \sum |F_o|, wR_2 = \{\sum w[(F_o)^2 - (F_c)^2]^2 / \sum w[(F_o)^2]^2\}^{1/2}$$

Table S2 Selected bond lengths (Å) for **1** at three phases

α phase at 120 K			
Ni(1)–N(6)	2.064(4)	Ni(1)–N(5)	2.070(4)
Ni(1)–N(3)	2.081(4)	Ni(1)–N(4)	2.086(4)
Ni(1)–N(6)	2.094(3)	Ni(1)–N(6)	2.115(3)
β phase at 180 K			
Ni(1)–N(2)	2.064(2)	Ni(1)–N(1)	2.083(2)
Ni(1)–N(3)	2.093(2)	Ni(1)–N(4)	2.106(2)
γ phase at 296 K			
Ni(1)–N(2)	2.078(3)	Ni(1)–N(1)	2.113(4)

Table S3 The S...S contacts (Å) in **1** at three phases

α phase at 120 K			
S(3)...S(6)#1	3.462(2)	S(4)...S(5)#2	3.536(2)
S(1)...S(2)#3	3.594(2)		
β phase at 180 K			
S(2)...S(3)#4	3.553(1)	S(1)...S(4)#3	3.611(1)
γ phase at 296 K			
S(2)...S(2)#5	3.573(2)	S(1)...S(1)#6	3.632(2)

Symmetry code: #1. $1/2 + x, 3/2 - y, -1/2 + z$; #2. $1/2 + x, 3/2 - y, 1/2 + z$; #3. $1 + x, y, z$; #4. $x, 1 + y, z$; #5. $3/2 - x, y, 1/2 - z$; #6. $2 - x, 1 - y, 1 - z$.

Table S4 The fitting parameters of the doubly superimposed Havriliak–Negami equation for **1** at specific temperatures

T (K)	ϵ_{∞}	α_1	β_1	$\Delta\epsilon_1$	$\tau_{0,1}$ (s)	α_2	β_2	$\Delta\epsilon_2$	$\tau_{0,2}$ (s)	σ_{dc}
263	4.78	0	0.79	3.00	7.0×10^{-7}	-		-	-	-
273	4.71	0	0.73	3.04	4.2×10^{-7}	0	0.67	0.53	1.2×10^{-2}	4.4×10^{-11}
283	4.64	0	0.68	3.10	2.4×10^{-7}	0	0.66	0.76	8.6×10^{-3}	5.5×10^{-10}
293	4.54	0	0.63	3.21	1.6×10^{-7}	0	0.65	1.08	6.4×10^{-3}	1.5×10^{-9}
303	4.42	0	0.57	3.34	1.0×10^{-7}	0	0.65	1.63	4.5×10^{-3}	3.8×10^{-9}
313	4.30	0	0.49	3.49	7.0×10^{-8}	0	0.64	2.49	3.3×10^{-3}	9.5×10^{-9}

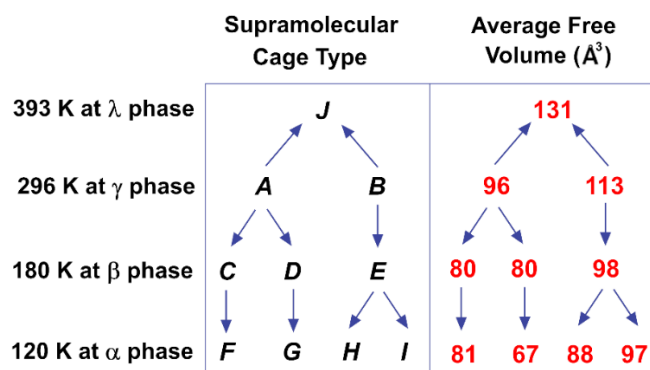


Chart S1 Evolution of the supramolecular cage types with variable free volumes (using a probe radius set as 2.4 \AA) in the four phases of **1**.

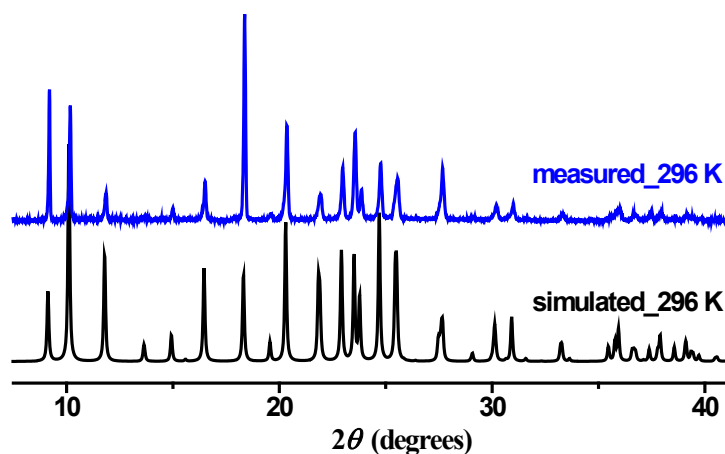


Fig. S1 Room-temperature powder XRD patterns of **1**.

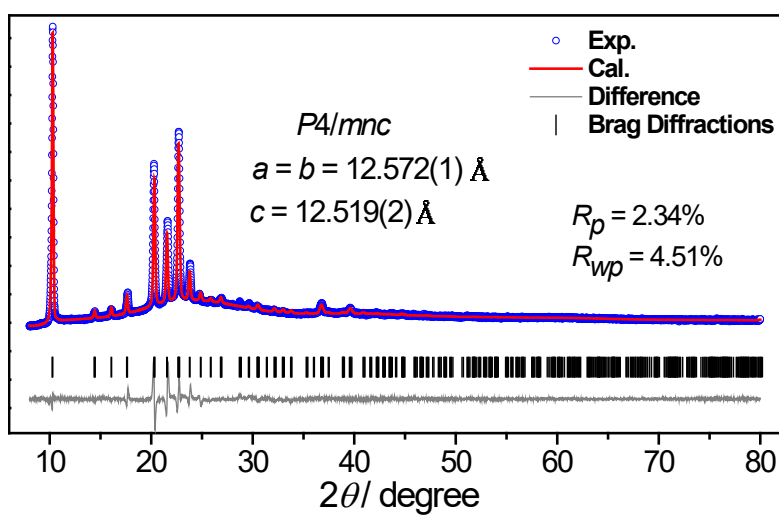


Fig. S2 Final Rietveld refinement result for **1 λ** phase at 393 K.

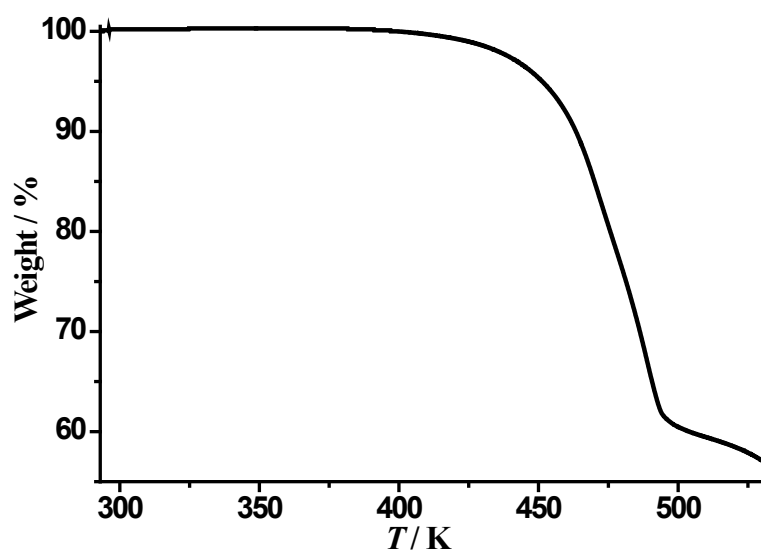


Fig. S3 Thermogravimetric curve of 1.

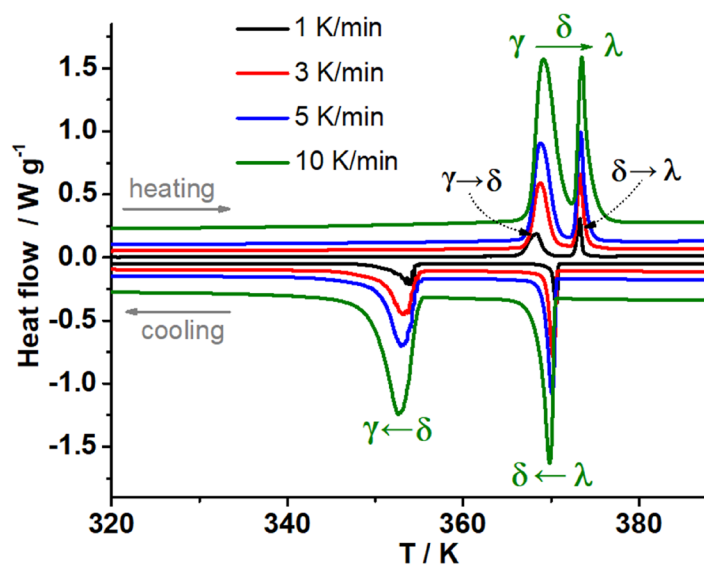


Fig. S4 In situ above-room-temperature DSC measurement for 1 recorded on variable heating/cooling rates of 1, 3, 5 and 10 K/min, respectively.

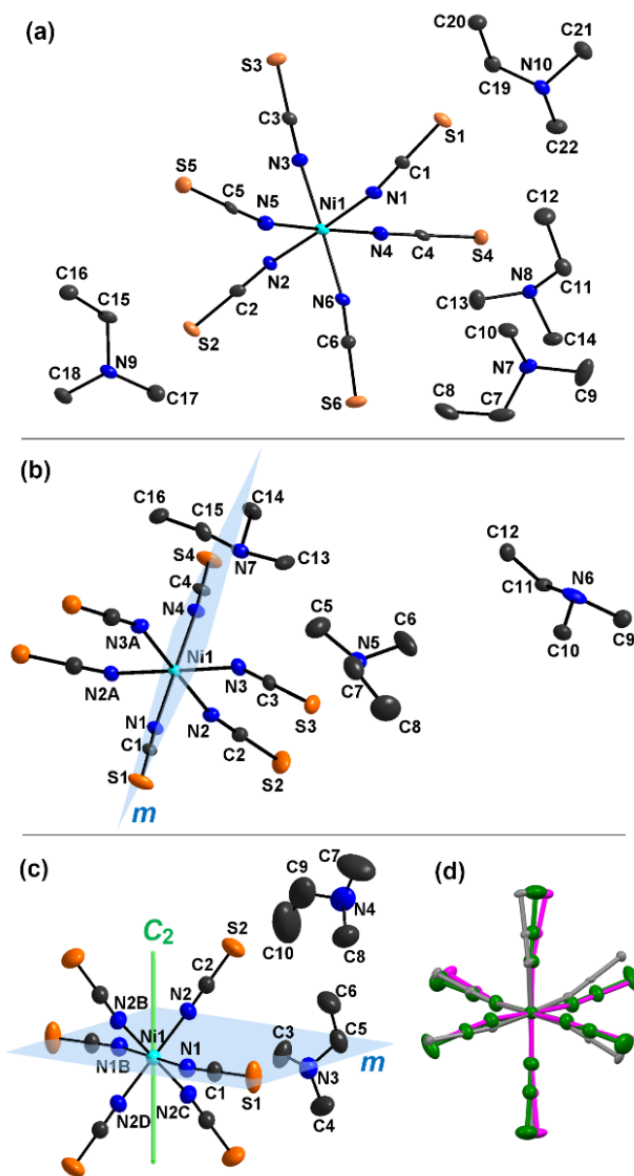


Fig. S5 ORTEP representations of the selected unit of **1** at 120 K (a), 180 K (b), and 296 K (c), respectively, with symmetry breaking and increasing thermal vibration amplitude. For the disordered Me₂EtNH⁺ ions in (b) and (c), only one orientation is shown for clarity. For comparison, the overlay map of the [Ni(NCS)₆]⁴⁻ anions in three phases is shown in (d), shaded in grey (120 K), purple (180 K), and green (296 K), respectively. Symmetry codes: A) $x, y, 1/2 - z$; B) $1 - x, 1 - y, z$; C) $x, y, 1 - z$; D) $1 - x, 1 - y, 1 - z$.

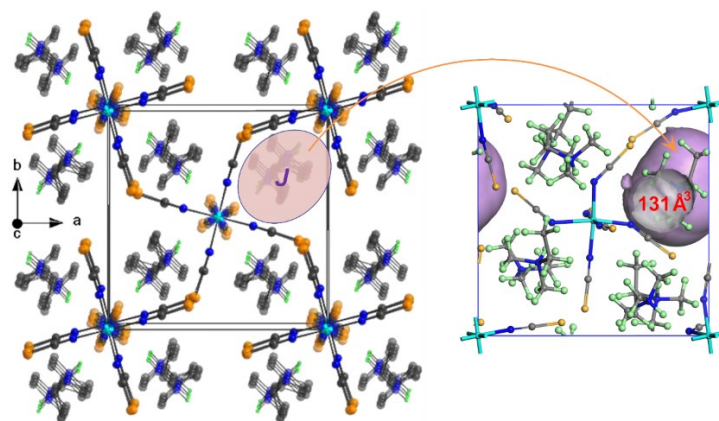


Fig. S6 View of the overall stacking in **1λ** phase. The disordered $\text{Me}_2\text{EtNH}^+/\text{[Ni(NCS)}_6\text{]}^{4-}$ ions are shaded in transparent. The N4-containing Me_2EtNH^+ ions reside in the supramolecular cage **J**. For display details, see Fig. 2.

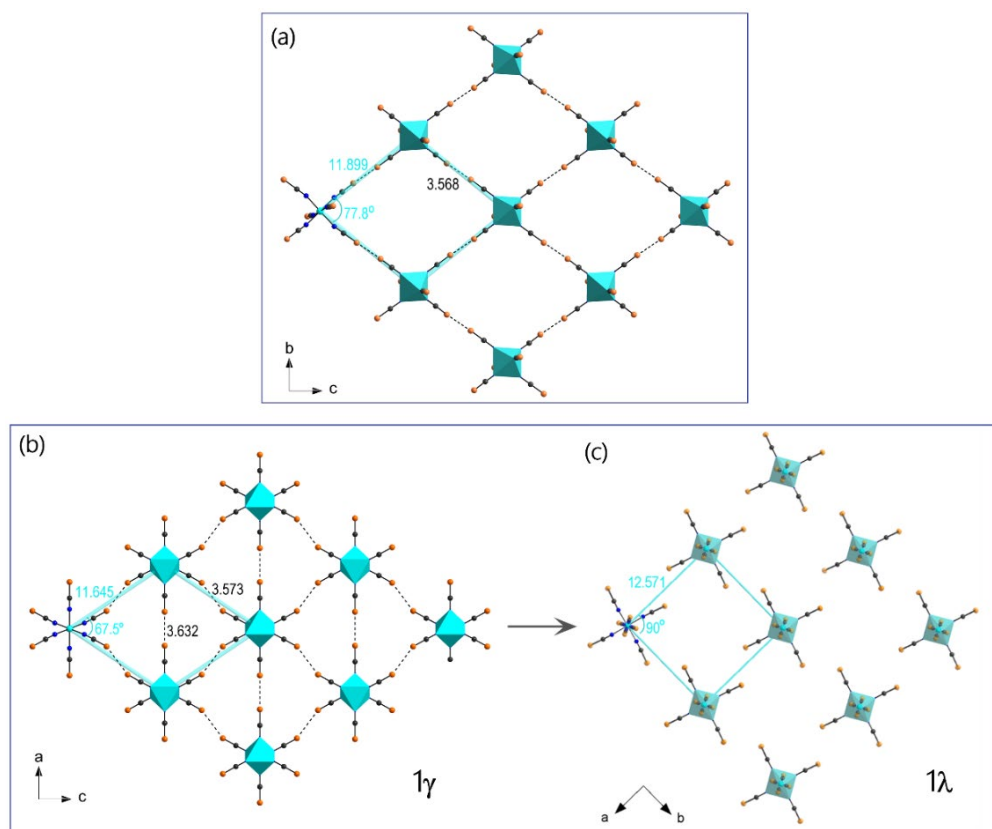


Fig. S7 Comparison of the room-temperature supramolecular $\{\text{[Ni(NCS)}_6\text{]}^{4-}\}_\infty$ layers in $(\text{Me}_3\text{NH})_4\text{[Ni(NCS)}_6\text{]}$ (a) and **γ** (b). The $\text{S}\cdots\text{S}$ contacts are represented by dashes. From **1γ** to **1λ**, the supramolecular $\{\text{[Ni(NCS)}_6\text{]}^{4-}\}_\infty$ layer is broken and the $\text{[Ni(NCS)}_6\text{]}^{4-}$ anions turn disordered dynamically. The significantly changed geometric arrangement of the $\text{[Ni(NCS)}_6\text{]}^{4-}$ anions is shown in (c).

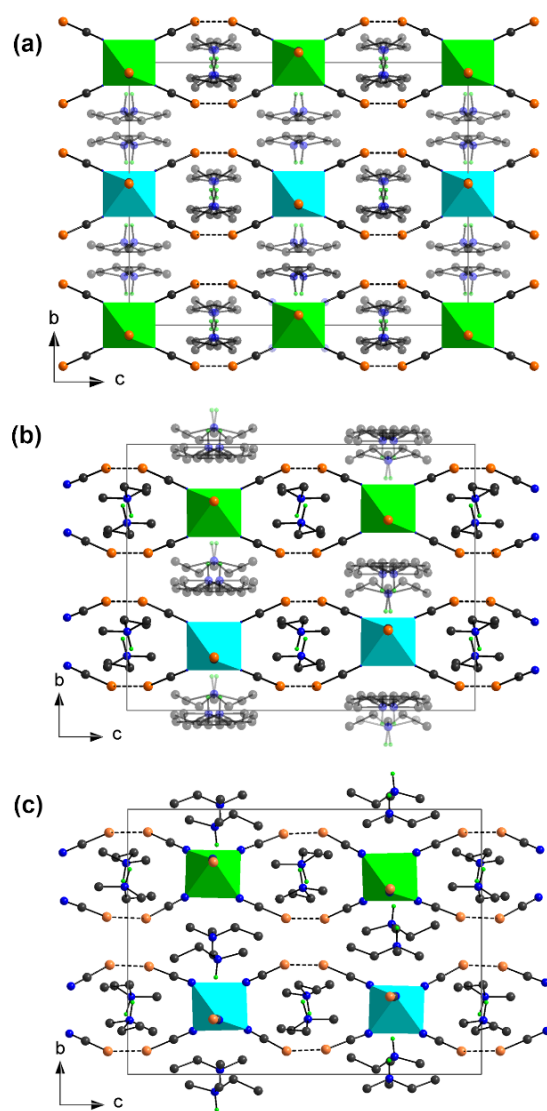


Fig. S8 Views of the overall stacking of **1 γ** (a), **1 β** (b) and **1 α** phases (c), respectively. The disordered Me_2EtNH^+ ions are shaded in transparent.

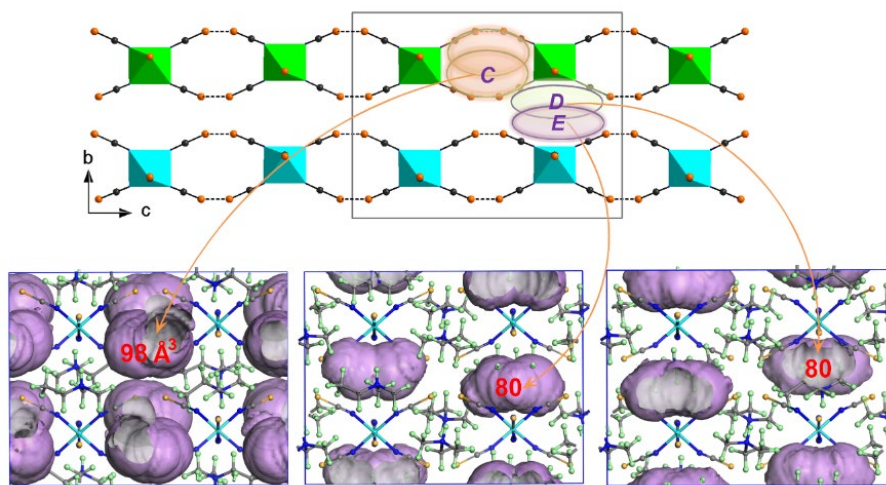


Fig. S9 Views of the stacking of the supramolecular layers of $[\text{Ni}(\text{NCS})_6]^{4-}$ anions in **1 β** phase (180 K) down the a -axis. The N5-, N6- and N7-containing Me_2EtNH^+ ions reside in the supramolecular cages **C**, **D** and **E**, respectively. For display details, see Fig. 2.

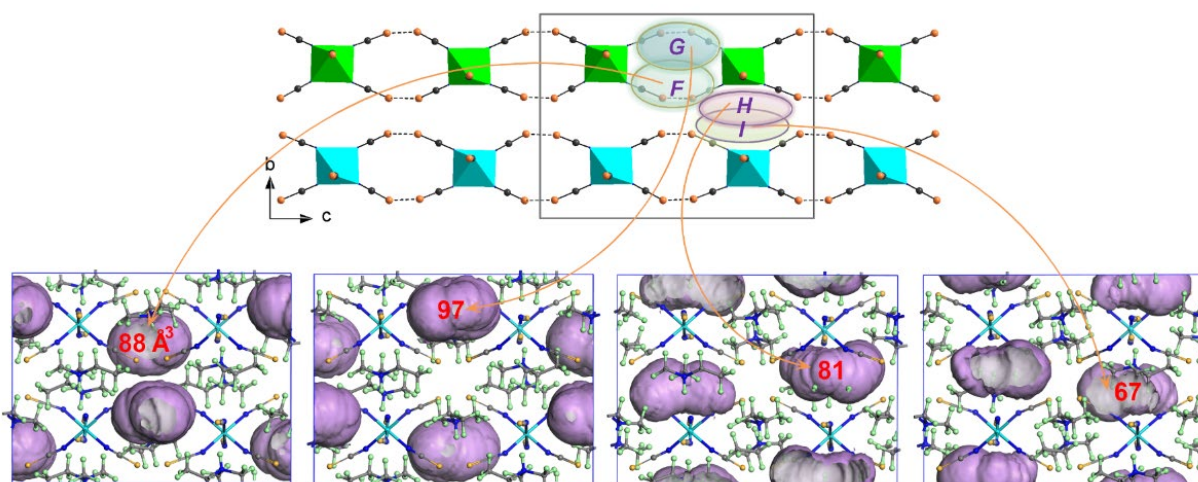


Fig. S10 Views of the stacking of the supramolecular layers of $[\text{Ni}(\text{NCS})_6]^{4-}$ anions in **1 α** phase (120 K) down the a -axis. The N7-, N8-, N9- and N10-containing Me_2EtNH^+ ions reside in the supramolecular cages **F**, **G**, **H** and **I**, respectively. For display details, see Fig. 2.

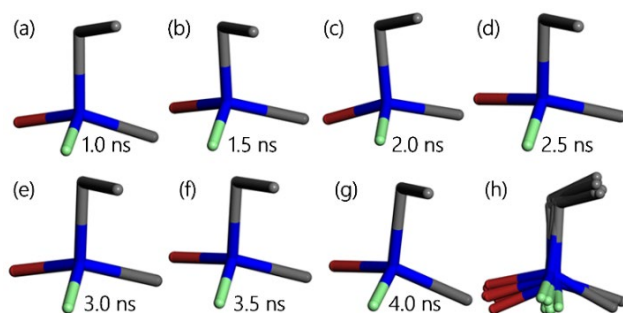


Fig. S11 Local snapshots of NVT dynamic simulation at 120 K for N7-containing Me_2EtNH^+ ion in 1α phase over the simulation time (a-g), and the overlapping maps of these snapshots (h). All C-bound H atoms are omitted for clarity.

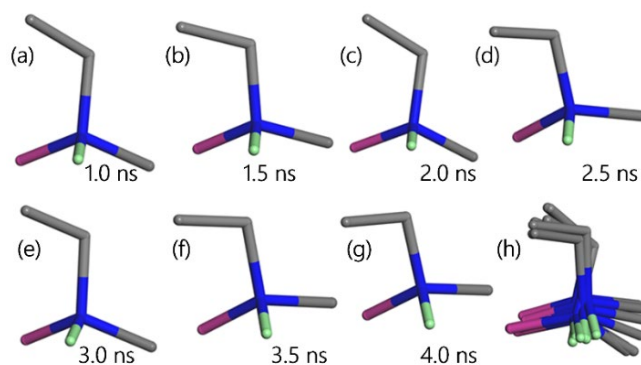


Fig. S12 Local snapshots of NVT dynamic simulation at 120 K for N8-containing Me_2EtNH^+ ion in 1α phase over the simulation time (a-g), and the overlapping maps of these snapshots (h).

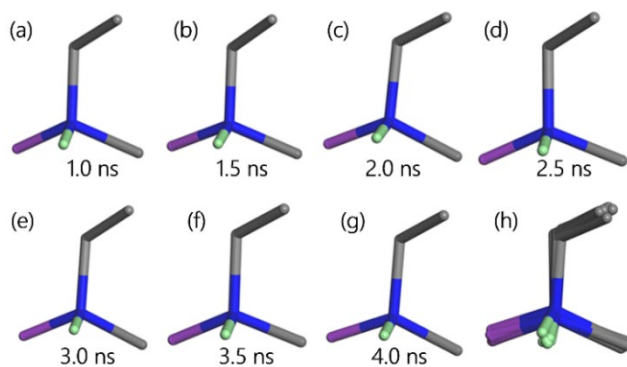


Fig. S13 Local snapshots of NVT dynamic simulation at 120 K for N9-containing Me_2EtNH^+ ion in 1α phase over the simulation time (a-g), and the overlapping maps of these snapshots (h).

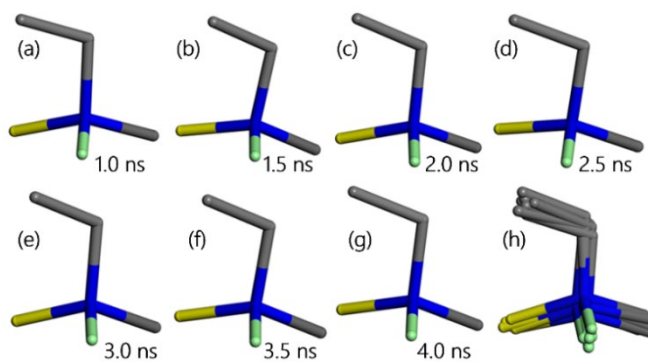


Fig. S14 Local snapshots of NVT dynamic simulation at 120 K for N10-containing Me_2EtNH^+ ion in 1α phase over the simulation time (a-g), and the overlapping maps of these snapshots (h).

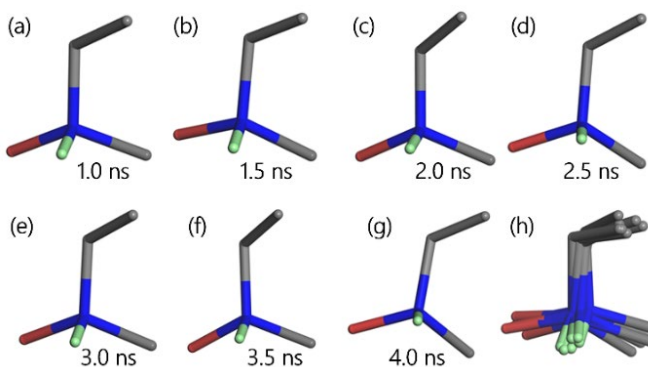


Fig. S15 Local snapshots of NVT dynamic simulation at 180 K for N5-containing Me_2EtNH^+ ion in 1β phase over the simulation time (a-g), and the overlapping maps of these snapshots (h).

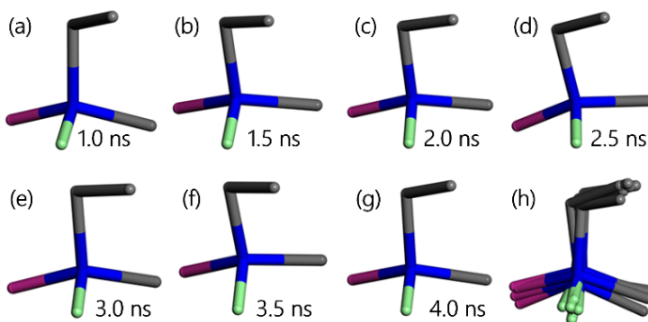


Fig. S16 Local snapshots of NVT dynamic simulation at 180 K for N6-containing Me_2EtNH^+ ion in 1β phase over the simulation time (a-g), and the overlapping maps of these snapshots (h).

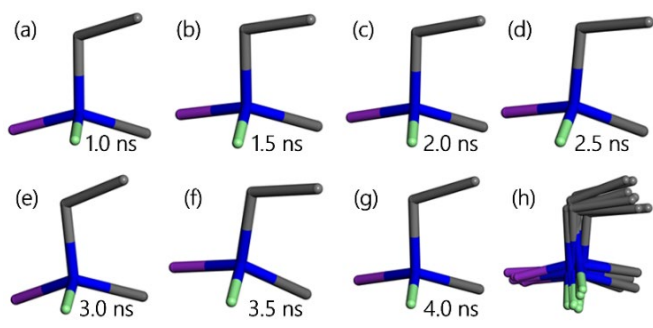


Fig. S17 Local snapshots of NVT dynamic simulation at 180 K for N7-containing Me_2EtNH^+ ion in 1β phase over the simulation time (a-g), and the overlapping maps of these snapshots (h).

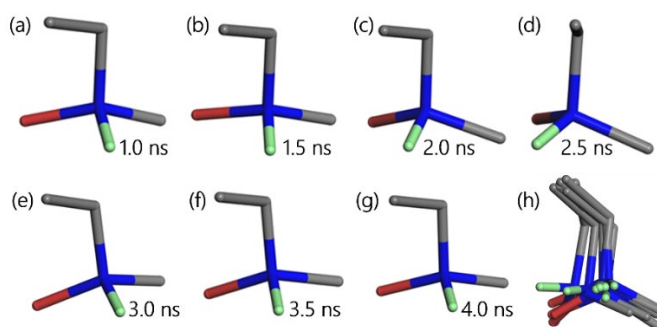


Fig. S18 Local snapshots of NVT dynamic simulation at 300 K for N3-containing Me_2EtNH^+ ion in 1γ phase over the simulation time (a-g), and the overlapping maps of these snapshots (h).

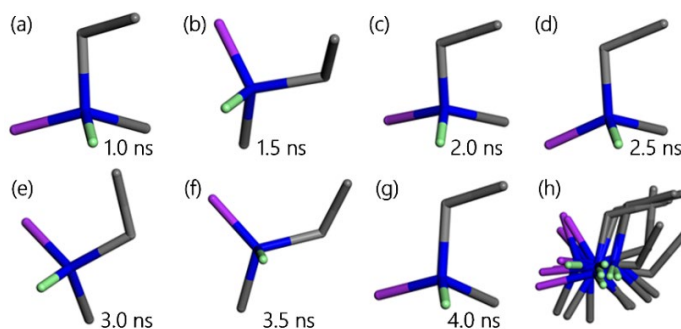


Fig. S19 Local snapshots of NVT dynamic simulation at 300 K for N4-containing Me_2EtNH^+ ion in 1γ phase over the simulation time (a-g), and the overlapping maps of these snapshots (h).

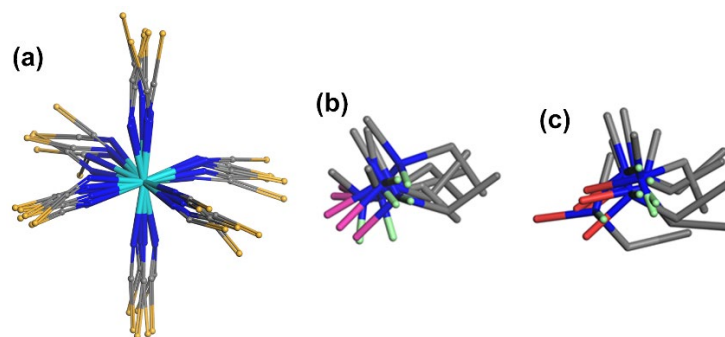


Fig. S20 Overlapping maps of the snapshots for one $[\text{Ni}(\text{NCS})_6]^{4-}$ anion (a) and two N3-containing Me_2EtNH^+ ions (b, c), respectively, by first-principles NVT dynamic simulation of 1λ phase at simulation temperature of 573 K, showing orientation changes and short-range displacements over the simulation time of 0, 2, 4, 6, 8, and 10 ps.

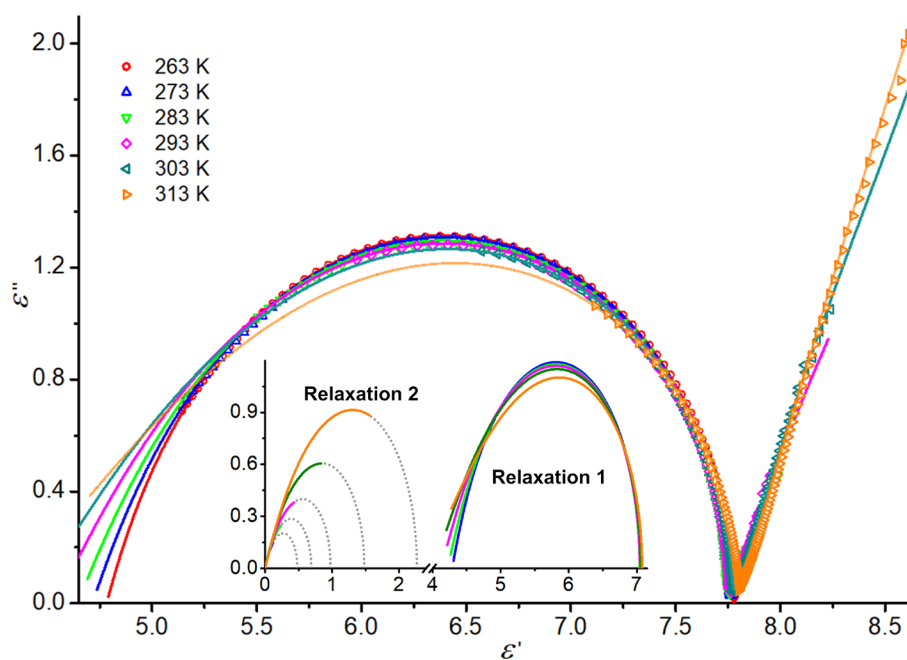


Fig. S21 The variable-temperature Cole-Cole plots as a series of arcs shown the relationship between ϵ' and ϵ'' . Based on the obtained fitting parameters, the fitted Cole-Cole diagrams of two separated relaxation processes 1 and 2 are illustrated in the inset map.

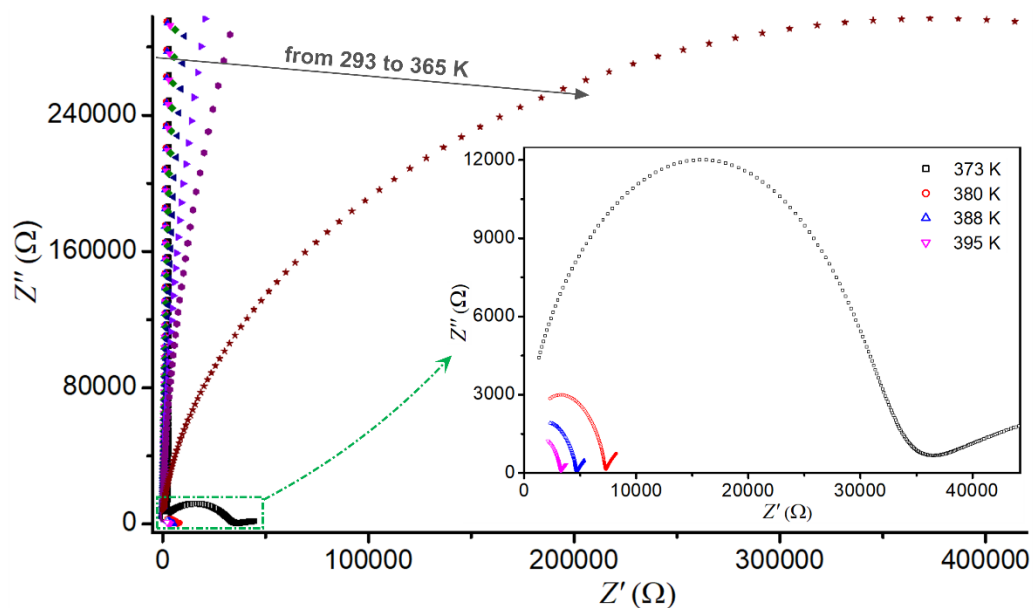


Fig. S22 Variable-temperature impedance spectra for the polycrystalline pellet of **1** in the temperature range from 293 to 395 K.

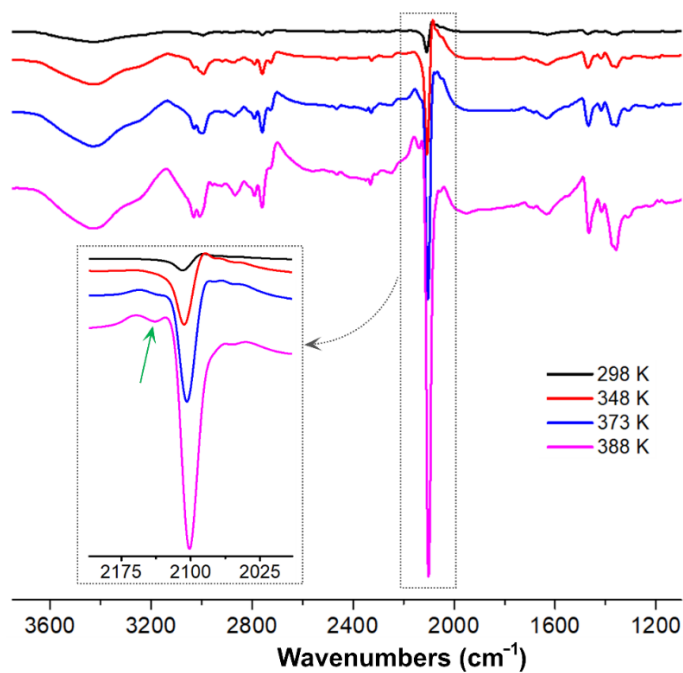


Fig. S23 Variable-temperature infrared spectra of **1** in the temperature range from 298 to 388 K.